



Delft University of Technology

Ultra-low-noise microwave to optics conversion in gallium phosphide

Stockill, Robert; Forsch, Moritz; Hijazi, Frederick; Beaudoin, Grégoire; Pantzas, Konstantinos; Sagnes, Isabelle; Braive, Rémy; Gröblacher, Simon

DOI

[10.1038/s41467-022-34338-x](https://doi.org/10.1038/s41467-022-34338-x)

Publication date

2022

Document Version

Final published version

Published in

Nature Communications

Citation (APA)

Stockill, R., Forsch, M., Hijazi, F., Beaudoin, G., Pantzas, K., Sagnes, I., Braive, R., & Gröblacher, S. (2022). Ultra-low-noise microwave to optics conversion in gallium phosphide. *Nature Communications*, 13(1), Article 6583. <https://doi.org/10.1038/s41467-022-34338-x>

Important note

To cite this publication, please use the final published version (if applicable).
Please check the document version above.

Copyright

Other than for strictly personal use, it is not permitted to download, forward or distribute the text or part of it, without the consent of the author(s) and/or copyright holder(s), unless the work is under an open content license such as Creative Commons.

Takedown policy

Please contact us and provide details if you believe this document breaches copyrights.
We will remove access to the work immediately and investigate your claim.

Ultra-low-noise microwave to optics conversion in gallium phosphide

Received: 13 April 2022

Accepted: 21 October 2022

Published online: 03 November 2022



Robert Stockill^{1,2,6}, Moritz Forsch^{1,6}, Frederick Hijazi^{1,2}, Grégoire Beaudoin³, Konstantinos Pantzas³, Isabelle Sagnes³, Rémy Braive^{3,4,5} & Simon Gröblacher^{1,2}✉

Mechanical resonators can act as excellent intermediaries to interface single photons in the microwave and optical domains due to their high quality factors. Nevertheless, the optical pump required to overcome the large energy difference between the frequencies can add significant noise to the transduced signal. Here we exploit the remarkable properties of thin-film gallium phosphide to demonstrate bi-directional on-chip conversion between microwave and optical frequencies, realized by piezoelectric actuation of a Gigahertz-frequency optomechanical resonator. The large optomechanical coupling and the suppression of two-photon absorption in the material allows us to operate the device at optomechanical cooperativities greatly exceeding one. Alternatively, when using a pulsed upconversion pump, we demonstrate that we induce less than one thermal noise phonon. We include a high-impedance on-chip matching resonator to mediate the mechanical load with the 50-Ω source. Our results establish gallium phosphide as a versatile platform for ultra-low-noise conversion of photons between microwave and optical frequencies.

The physical carrier of quantum information plays a crucial role in how the information is processed, communicated and measured. Encoding quantum information in microwave-frequency photons has allowed for the development of circuit¹ and spin-based^{2,3} quantum information processing. At the same time, optical photons at telecom wavelength are a natural carrier for quantum information⁴, benefitting from particularly low loss rates in optical fibers⁵, an effectively noise-free environment at room temperature and near-unity efficiency single-photon detection technology⁶.

Bridging the five-orders-of-magnitude frequency difference between the microwave and optical domains will allow for flexible manipulation and communication of quantum information^{7–9}, enabling both networked quantum computation and complex processing of long-range entangled states. Steady progress in various experimental realizations of such microwave-to-optics converters has been achieved in the past few years¹⁰, with significant challenges

remaining. These include low-noise operation, efficient transduction, and the construction of scalable platforms. In particular, the requirement of an optical-frequency pump to compensate for the large frequency mismatch introduces the possibility of absorption-based noise which can overwhelm the ultra-low power signal and corrupt the quantum information.

Owing to weak electro-optic coupling rates, the large optical pump powers required for efficient operation typically prohibit direct conversion without the addition of significant absorption-induced noise¹¹. An alternative is to find intermediaries which can reduce the required optical pump size, while at the same time providing high-cooperativity interfaces to both electrical and optical domains, a role for which mechanical resonators are an attractive system^{12–18}. To this end, the interaction between a mechanical oscillator and a co-localized optical mode has enabled the creation and measurement of nonclassical states of motion^{19–21}. At the same time, by using the

¹Kavli Institute of Nanoscience, Department of Quantum Nanoscience, Delft University of Technology, 2628CJ Delft, The Netherlands. ²QphoX B.V., 2628XG Delft, The Netherlands. ³Centre de Nanosciences et de Nanotechnologies, CNRS, Université Paris-Saclay, C2N, 91767 Palaiseau, France. ⁴Université Paris-Cité, 75006 Paris, France. ⁵Institut Universitaire de France (IUF), Paris, France. ⁶These authors contributed equally: Robert Stockill, Moritz Forsch.

✉ e-mail: s.groblacher@tudelft.nl

piezoelectric interaction or mechanical modification of resonator capacitances mechanical modes have been successfully interfaced with excitations in superconducting qubits^{22,23}. A recent demonstration has shown the generation of optical photons from a superconducting qubit embedded within a transducer²⁴, however the close proximity of the transducer to the qubit resulted in the production of quasi-particles in the superconductor, disturbing the qubit coherence. The realization of a stand-alone quantum transducer, which could in turn be connected to a shielded quantum system, remains an ongoing challenge.

Gallium phosphide (GaP) combines a high refractive index ($n_{\text{GaP}} = 3.1$) and a large band gap (2.3 eV) with a non-centro-symmetric crystal structure enabling applications for low-loss integrated photonics in the telecom band²⁵. Thanks to the suppressed two-photon absorption of telecom-wavelength light and the intrinsic piezoelectric coupling in GaP, the material has shown promise in a demonstration of nonclassical optomechanics²⁶ as a suitable host for a full microwave-to-optical transducer.

Here we build on the impressive properties of GaP (for more details see *Methods*) and realize microwave-to-optics conversion using this material. We enhance our previously demonstrated optics-to-mechanical interface with an electrical-to-mechanical interface, whereby we directly actuate a breathing mode of the optomechanical resonator. We include an impedance matching network to mediate the high-impedance load presented by the mechanical resonance with a 50- Ω source²⁷. The ultra-low absorption of telecom photons in the material enables operation of the device with optomechanical cooperativities $C_{\text{om}} \gg 1$ under continuous driving. For pulsed operation, we demonstrate total conversion efficiencies of 6.8×10^{-8} , featuring a mechanical-to-optical efficiency of 1.9×10^{-2} (see *Methods*), while maintaining a thermal occupation in the nanobeam mechanical mode of only $n_{\text{th}} = 0.55 \pm 0.05$ phonons.

Results

Our converter consists of an optomechanical and an electro-mechanical interface (Fig. 1a). The former is realized by a nanobeam optomechanical crystal (OMC)²⁸, with an optical resonance around 1550 nm and a mechanical breathing mode (Fig. 1d) with a resonance frequency of $\omega_m = 2\pi \times 2.81$ GHz. We fabricate our devices out of a 230-nm-thick layer of suspended gallium phosphide²⁹. The electro-mechanical interface is realized by a piezoelectric resonator with a breathing mode of the same symmetry and polarisation as the nanobeam mode (Fig. 1d). These two interfaces are mechanically connected and are brought into resonance by careful design of the width of the piezoelectric resonator. In order to facilitate the mechanical coupling between the two parts of the converter, we design the OMC such that the mechanical mode can leak out of the resonator³⁰. We attach the converter to its surrounding through an acoustic shield^{21,31} to avoid an increased mechanical decay rate into the environment. A direct benefit of this approach is that we can spatially separate the optical cavity from the metallic electrodes, which avoids perturbations of the optical resonance as well as negative effects on the superconducting electrodes due to a nearby optical cavity.

The actuation of the piezoelectric resonator's breathing mode is facilitated by alignment of the device axis (Fig. 1d) with the [110] axis in the zincblende lattice of gallium phosphide. For this orientation, the breathing mode of the piezoelectric resonator produces an out-of-plane electric field (bottom of Fig. 1d). We use a coplanar-waveguide electrode configuration to produce this field orientation and actuate the mechanical mode, which results in a simulated piezoelectric coupling strength for the piezo-resonator alone of $k_{\text{eff}}^2 = 1.59 \times 10^{-6}$ (see *Methods*). While the small physical size of the piezoelectric resonator is compatible with large optomechanical coupling rates, the resulting small simulated capacitance of $C_{\text{res}} = 0.17$ fF results in a large electrical impedance (see *Methods*, we expect $R_m = 2.1$ M Ω for a mechanical

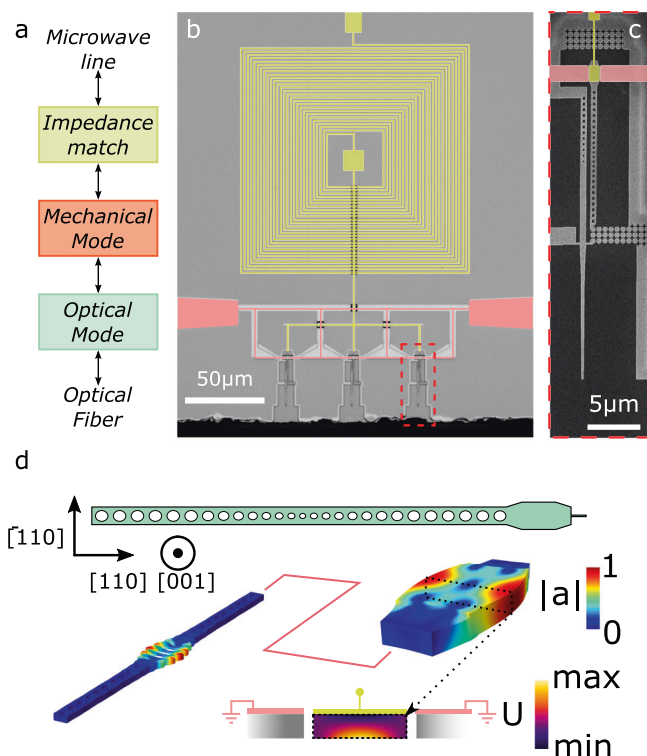


Fig. 1 | Conversion device. **a** Schematic showing the mechanically-mediated conversion process between microwave and optical frequencies. **b** Microscope image of the full device consisting of a spiral inductor (top) and three nanobeam OMCs (bottom). Only one of the OMCs is used at any one time. The image is overlaid with false coloring to clarify the ground (red) and center conductor (yellow). **c** Zoom-in to one of the nanobeam OMCs. The optical cavity in the nanobeam is evanescently coupled to the optical waveguide, to which we couple with a lensed fiber. The nanobeam is mechanically connected to the piezoelectric resonator and the whole structure is secured to the environment through acoustic shielding. **d** Illustration of the combined electro-opto-mechanical converter and the relevant coordinate system (top). Simulated breathing modes of the OMC (left) and piezoelectric resonator (right) around 2.8 GHz. The breathing mode is coupled to an out-of-plane electric potential gradient (bottom, center block, see *Methods*), which we induce with the coplanar electrodes.

quality factor of 100,000), such that conversion from a 50 Ω coaxial line is very inefficient. To overcome this challenge we pattern an electrical impedance-matching circuit on the chip, consisting of a spiral inductor fabricated from a 90-nm-thick layer of molybdenum rhenium (MoRe) (Fig. 1b)³². The capacitance of the impedance matching circuit is limited by the parasitic capacitance of the spiral to ground. In order to match a high-Z impedance, the characteristic impedance of the matching circuit, Z_{match} , should be large, while the resonance frequency should be matched to the mechanical resonance $\omega_{\text{match}} = \omega_m$. For resonant circuits we extract a circuit impedance of $Z_{\text{match}} = 3.1$ k Ω , suitable for matching a load of 192 k Ω to a 50 Ω source.

Characterization

We fabricate the device shown in Fig. 1b and cool it to Millikelvin temperatures in a dilution refrigerator to initialize the mechanical mode into its ground state. First, we record a reflection spectrum of the optical cavity by scanning a tunable laser across the resonance. The spectrum reveals a mode at $\lambda_c = 1555.4$ nm ($\omega_c = 2\pi \times 192.743$ THz) with a linewidth (FWHM) of $\kappa = 2\pi \times 4.17$ GHz, over-coupled to the optical waveguide with external coupling rate $\kappa_e = 2\pi \times 2.54$ GHz (see *Methods*).

We then proceed to characterize the mechanical modes of interest. We identify these modes by performing an electro-optic S21 measurement, where we use a vector network analyzer (VNA) to

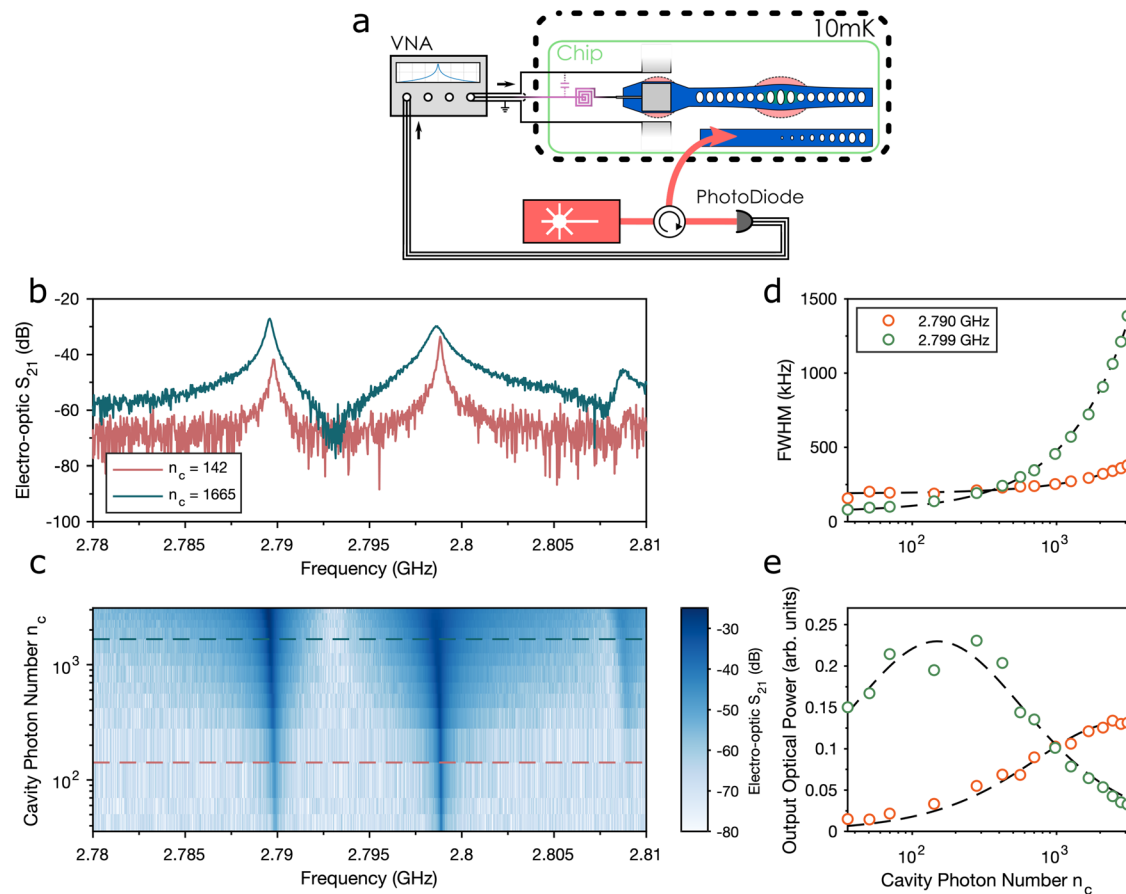


Fig. 2 | Device characterization using an electro-optic S21 measurement.

a Setup for continuous conversion measurement. The device is driven by the output of a vector network analyzer (VNA). The mechanical mode is then read out using a CW laser which is red-detuned from the optical cavity by $-\omega_m$. The reflected light is then recorded on a high-frequency photodiode and the signal fed back to the VNA. **b** Electro-optic conversion signal around 2.8 GHz. Red

(blue) curve taken for $n_c = 142$ (1665). In this electro-optic S21 spectrum, we can see two prominent modes at 2.790 GHz and 2.799 GHz. **c** Power-dependent electro-optic conversion signal. **d** Conversion linewidth for varying optical cavity photon number. Green (orange) points are for the mode at 2.799 (2.790) GHz. **e** Photon-number-dependent un-normalized optical output power for the same two modes.

provide an RF-drive tone to the electrical input of the device which excites the mechanical modes. At the same time, we use a laser stabilized to the red sideband of the optomechanical cavity ($\omega_l = \omega_c - \omega_m$) to upconvert the signal which we monitor in the high-frequency noise of the reflected light using a high-frequency photodetector. The setup is displayed in Fig. 2a. The resulting spectrum is shown in Fig. 2b, where we can identify two efficient modes at 2.790 GHz and 2.799 GHz. We perform an electrical S11 reflection measurement of the impedance matching resonator, which reveals a resonance at 2.85 GHz, 50 MHz blue-detuned from the relevant mechanical modes (see *Methods*). Further, we confirm the bi-directional nature of the transduction process by measuring downconversion from the microwave to optical domain (see *Methods*).

Continuous conversion

We obtain insight into the optomechanical device operation by performing conversion while sweeping the input optical power. The electro-optic signal for a range of optical cavity photon numbers (n_c) is plotted in Fig. 2c. From fits to the two most efficient frequencies, we extract the transduction bandwidth and un-normalized output optical power, displayed in Fig. 2d and e, respectively. For larger optical-cavity photon numbers we observe a linear increase in the transduction bandwidth for both modes, owing to optomechanical damping. We use this increase in damping rate to extract the single-photon optomechanical coupling rates for the two modes (see *Methods*), from which we find a value of $g_0 = 2\pi \times 700 \pm 8$ kHz ($2\pi \times 272 \pm 14$ kHz) for

the mode at 2.799 GHz (2.790 GHz). We also extract the intrinsic damping rate of the mechanical modes, γ_m , from these fits, and find a rate of $\gamma_m = 2\pi \times 67 \pm 8$ kHz ($\gamma_m = 2\pi \times 191 \pm 14$ kHz) for the 2.799 GHz (2.790 GHz) mode, resulting in a single photon cooperativity (defined as $C_0 = 4g_0^2/\kappa\gamma_m$) of $C_0 = (7.0 \pm 0.81) \times 10^{-3}$ ($C_0 = (3.7 \pm 0.5) \times 10^{-4}$).

We plot the evolution of the output optical power in Fig. 2e. We recover peaked transduction efficiencies with maximum values for the 2.799 GHz (2.790 GHz) mode at 148 (2720) photons in the optical cavity, corresponding to optomechanical cooperativities of 1.04 (1.01), in good agreement with the expected behaviour $\eta_{om} \propto C_{om}/(1+C_{om})^2$, where $C_{om} = n_c C_0$. We reach unity cooperativity for an incident optical power of 0.5 μ W (11.3 μ W). While the relatively low electromechanical cooperativity of the device prevents us from directly measuring the absolute electromechanical coupling rate, we can determine that the electro-mechanical coupling rate for the 2.790 GHz mode is around three times larger than the 2.799 GHz mode. This difference suggests that the higher frequency mode is predominantly located in the opto-mechanical resonator, and the lower frequency mode in the piezo-resonator.

We note that we are able to record reproducible efficiency results over this wide range of optomechanical cooperativities thanks to the absence of two-photon absorption-induced thermo-optic bistability in GaP²⁹. These results also demonstrate the lack of significant damage to the superconducting metal circuitry for these operating powers.

While the measurements shown in Fig. 2 already confirm microwave-to-optics conversion with this device, the continuous operation in this experiment is accompanied by an elevated thermal

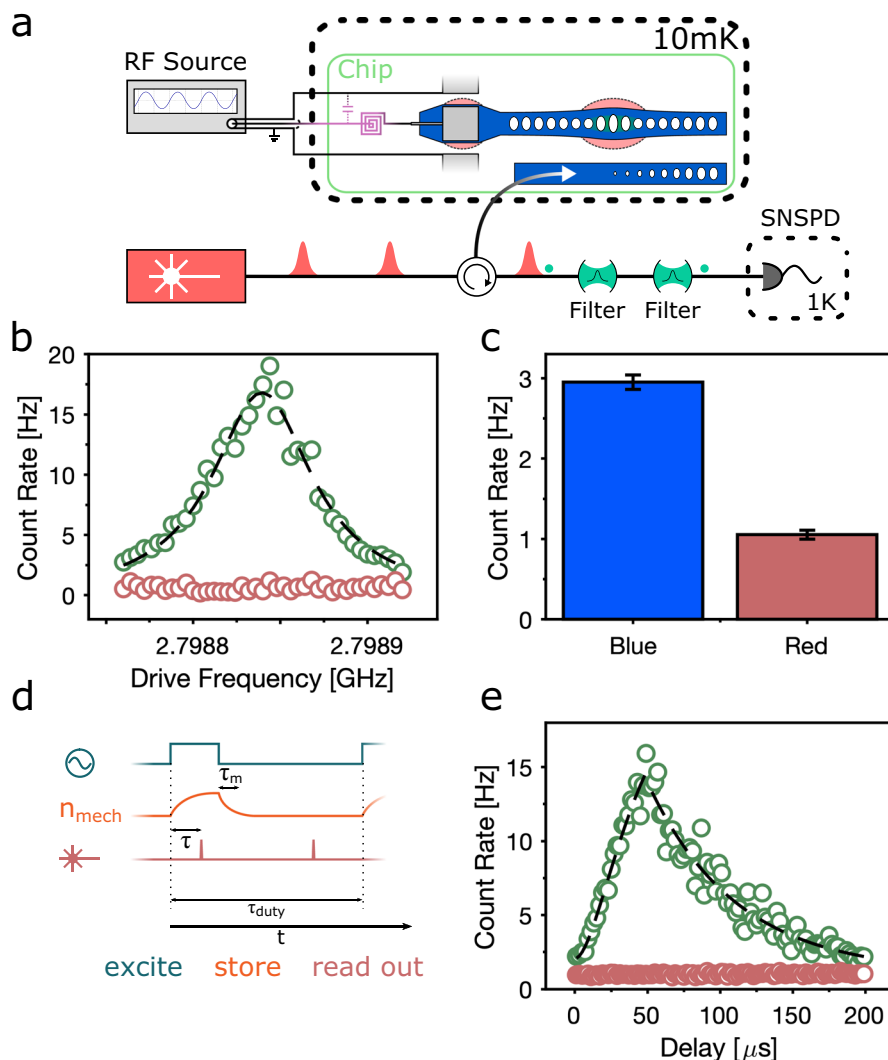


Fig. 3 | Pulsed conversion. **a** Microwave-to-optics conversion measurement setup. We first excite the mechanical mode with a square microwave pulse and then probe the population of the mechanical mode using an optical pulse on the red sideband of the optomechanical cavity ($\omega_l = \omega_c - \omega_m$). We then filter out residual pump light and detect the remaining cavity-resonant photons on SNSPDs. **b** Frequency sweep of the pulsed microwave drive across the lowest mechanical resonance. We send a microwave pulse with length 26 μ s, followed by a 40 ns optical pulse to probe the mode occupation (green datapoints). We let the mode fully re-thermalize again before sending another red-detuned pulse to obtain a base-count rate corresponding to the thermal background (red data points). The green datapoints are overlaid with a Lorentzian fit with a linewidth of $2\pi \times 67$ kHz. **c** Sideband asymmetry measurement without an RF-drive. Here, we send a sequence of red(blue)-detuned pulses to the device, spaced in time by several mechanical lifetimes. The red (blue)

pulses realize the beamsplitter (two-mode squeezing Hamiltonian) and result in count rates $\Gamma_R \propto n_{\text{th}}(\Gamma_B \propto n_{\text{th}} + 1)$. Error bars are s.d. **d** Schematic illustration of our conversion process. We excite the mode using a square microwave pulse (teal). This pulse leads to a buildup of the mechanical mode's population (orange). After the end of the microwave pulse, the mode population decays with the lifetime of the mode, $\tau_m = 61.4$ μ s. We probe the occupation of the mechanical mode using a red-detuned optical pulse. By setting the delay of this pulse with respect to the beginning of the square pulse, we can trace out the evolution of the mechanical mode's population. We also use a second optical probe pulse after the mechanical mode has decayed in order to measure a reference count rate for an empty mode. **e** Time dynamics of the mechanical mode population. Green datapoints show the integrated count rate over the duration of the optical pulse. Dashed curves are fits to the rising and decaying cavity population¹⁵.

occupation of the mechanical mode. Therefore, it is important to investigate the performance of this device in the context of the desirable low-noise regime which is crucial for quantum applications. By operating both the microwave drive and the optical interface in a pulsed fashion, we can reduce the thermal noise of the mechanical mode and access the photon-number conversion efficiency. In the following, we will restrict the discussion to the most efficient mode at 2.799 GHz.

Pulsed conversion

The basic elements of our setup for pulsed operation are displayed in Fig. 3a. We up-convert the phonons in the mechanical mode to the optical domain with 40-ns long red-detuned optical pulses

(at frequency $\omega_l = \omega_c - \omega_m$), separated by sufficient time for the mechanical mode to fully re-thermalize to the mK-environment. These short pulse lengths ensure that we can swap out the mechanical excitation into the optical mode before excess absorption-induced heating commences. We then filter out the upconverted photons from our reflected pump with two Fabry-Pérot filter cavities in series and detect the converted photons on superconducting nanowire single-photon detectors (SNSPDs).

We first find the conversion resonance again by scanning the input microwave frequency and monitoring the rate of single photon clicks, the result displayed in Fig. 3b, which shows the count rate with (green) and without (red) a 26- μ s-long microwave pulse. We also determine the thermal population of the mode under the same optical pulse

energy, by measuring the asymmetry between Stokes and anti-Stokes scattering for blue- and red-detuned laser pulses, respectively. The rates are shown in Fig. 3c, which corresponds to a value of $n_{\text{th}} = 0.55 \pm 0.05$ for the 40-fJ (314,000-photon) optical pulse energies used here. With separate measurements of the optomechanical coupling rate, we find that for these pulse energies, we convert phonons to optical photons with an efficiency of $p_{\text{sw}} = 3.2\%$. We note that during the optical pulse the optomechanical cooperativity (defined as $C = 4n_{\text{ph}}g_0^2/\kappa\gamma_m$, where n_{ph} is the number of photons present in the optical mode due to the pump pulse) exceeds unity, namely $C = 1.74$.

To measure the efficiency of our conversion process in the pulsed scheme, we follow the schedule in Fig. 3d. We first excite the mechanical mode with a square microwave-frequency pulse. We then upconvert the mechanical occupation to the optical domain with the 40-ns-long optical pulse. We choose this optical pulse length to swap out the mechanical state into the optical mode before excessive heating of the mechanical mode occurs. With a probability p_{sw} this pulse swaps the mechanical occupation into photons at the cavity resonance frequency, which leaks from the cavity into the coupled waveguide with an out-coupling efficiency of 61%. To find the highest efficiency, we scan the optical pulse along the duration of the microwave pulse, the results for a 50- μ s long microwave pulse are shown in Fig. 3e. For the mode analysed here, the maximum efficiency occurs for a pulse length of 26 μ s (as displayed in Fig. 3b). Taking into account external losses including attenuation of microwave lines and additional optical path losses, the latter we measure using the same scheme as in¹⁹, we estimate a total conversion efficiency of 6.8×10^{-8} . This can be broken up into a power-dependent mechanics-to-optics efficiency of 1.9×10^{-2} ($=p_{\text{sw}}\kappa_e/\kappa$), and an electrical-to-mechanical efficiency of 3.6×10^{-6} .

The mechanics-to-optics efficiency presented here is linearly dependent on the input optical pump energy, up to the limit of $\kappa_e/\kappa = \eta_0 = 0.61$. For smaller energies, the efficiency decreases, however, results in a better noise performance. If we operate in a regime where the mechanical-to-optical efficiency is 8×10^{-3} , we recover a mode population of $n_{\text{th}} = 0.36 \pm 0.03$ (see *Methods*). From the single photon cooperativity extracted from the data in Fig. 2, we can estimate the total single-pump-photon microwave-to-optical efficiency for the 2.799 GHz mode of 0.75×10^{-7} ¹⁶. We note that this is the highest per-optical-photon efficiency recorded for a standalone piezoelectric microwave-to-optics transducer.

The impedance of the piezoelectric interface drops for increasing mechanical quality factor, and it becomes easier to match to the 50 Ω source. While we record lifetimes for the mechanical mode of 61.4 μ s, which set an lower bound on the linewidth of $2\pi \times 2.5$ kHz (a quality factor of 1.08×10^6), due to mechanical frequency jitter, we recover a minimum linewidth for the mechanical mode of $\gamma_m = 2\pi \times 67$ kHz. This de-phasing effect is also visible in the time dynamics of the loaded mechanical mode we display in figure 3e, where the rise time of 16 μ s is significantly smaller than the decay time of the mechanical mode. This jitter reduces the efficiency with which we can load the mechanical mode, and raises the time-averaged electrical impedance of the mode. We estimate a reduction in the efficiency of 6.9 for quasi-static noise. Similarly increased linewidths have been observed in the mechanical resonances in silicon^{21,31}, and further studies are required to measure the dynamics of this noise source in GaP. Nonetheless, with higher matching circuit impedance, the electrically-enhanced mechanical damping rate would negate these effects. Another key component of the device efficiency is the detuning between the matching resonator and the mechanical mode. At milli-Kelvin temperatures, we measure a detuning between the matching network and the mechanical modes of 50–60 MHz. When we raise the temperature of the transducer to 4 K we red-shift the impedance matching resonance through the kinetic inductance of the MoRe film³², which compensates for the detuning and increases the efficiency by a factor of 2.2 and 1.7 for the 2.790 and 2.799 GHz modes, respectively. An alternative to temperature-tuning

of the kinetic inductance is magnetic field tuning, which can compensate for detunings of the order we observe here^{33,34}.

One route to higher electromechanical efficiency is through increasing the impedance of the matching circuit by minimizing stray circuit capacitance, which can be achieved through reduction in the size of the impedance matching coil, as well as undercutting of the circuit dielectric³⁵. Through these techniques, values of $C_{\text{match}} \sim 1\text{--}2$ fF are readily achievable, for which we expect to boost the electromechanical efficiency by two orders of magnitude. Alternatively, stronger piezoelectric materials, such as lithium-niobate, used in conjunction with silicon-on-insulator, would allow us to retain the optomechanical coupling rates we measure here, while increasing the electromechanical cooperativity²⁷. We note that recent demonstrations of mechanically-mediated transducers built entirely from stronger piezoelectric materials, such as all lithium niobate¹⁶ or aluminium nitride⁴⁵, have achieved higher overall efficiency. Nonetheless, these devices require significantly larger optical pump powers which prohibit efficient operation with sub-phonon thermal excitation.

Discussion

Our demonstration of conversion in gallium phosphide shows the material has great promise as the basis of a quantum-capable microwave-to-optics interface. To this end, we have demonstrated electromechanical coupling from a 50 Ω impedance source to an optically-coupled nanomechanical piezo-resonator through impedance matching. Thanks to the particularly low two-photon absorption in GaP, we operate the device in regimes where the optomechanical cooperativity greatly exceeds one, even in the pulsed regime and while keeping the mechanical oscillator in its ground state. Crucially for quantum transduction, we introduce sub-phonon noise levels during pulsed operation, while maintaining swap efficiencies between phonons and optical photons exceeding 0.05. In future work, the electromechanical coupling rate could be increased by using high-impedance electrical resonators^{33,35}, and the electromechanical cooperativity could be increased by decoupling the electrical resonator from the 50- Ω input. Further significant electromechanical efficiency increase can be expected from including a bottom electrode instead of our coplanar design, as was recently demonstrated in ref. 36 for GaP. Already with the current generation of devices we demonstrate a record-high single-pump-photon transfer efficiency for a standalone piezoelectric transducer, thanks to the large optomechanical coupling rate provided by the material.

During preparation of the manuscript, we became aware of related work demonstrating microwave-to-optics conversion in gallium phosphide³⁶.

Methods

Piezoelectric properties and orientation

Gallium phosphide is a III/V semiconductor that crystallizes in the cubic Zincblende lattice. Its piezoelectric properties arise from the small anisotropy given by the two different basis atoms: gallium and phosphorus. For the most common substrate orientation [001] ($\parallel \vec{z}$), the piezoelectric tensor describing these properties is given by:

$$e'_{jk}(\phi) = \frac{e_{14}}{2} \begin{bmatrix} 0 & 0 & 0 & 2a_2 & -2b_2 & 0 \\ 0 & 0 & 0 & 2b_2 & 2a_2 & 0 \\ -b_2 & b_2 & 0 & 0 & 0 & 2a_2 \end{bmatrix}, \quad (1)$$

where ϕ is the angle between the x -axis and the [110] direction, $a_2 = \sin(2\phi)$ and $b_2 = \cos(2\phi)$ ³⁷. For GaP, the value of e_{14} is -0.1C cm^{-2} ³⁸. Importantly, orienting our structures along the [110] ($\phi = 0$) axis results in non-zero values for e'_{31} and e'_{32} , which couple an out-of-plane electric field to X and Y strain, respectively, which allow us to realize this piezoelectrically active breathing mode of the block resonator. We access this vertical electric field through the coplanar electrodes

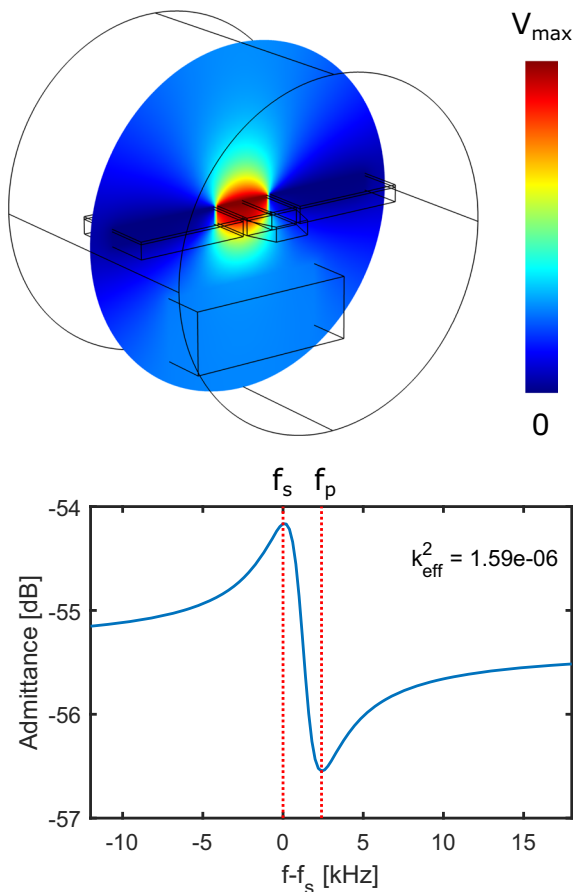


Fig. 4 | Electrical simulations of the Piezoelectric resonator. Top: stationary electrostatic simulation with a cut plane showing the electric potential. The cut plane is perpendicular to the [110] axis in the crystal. The simulated geometry consists of the piezoelectric resonator (center) with two tapered ends and two side pads. Both the resonator and the pads consist of a 230 nm-thick gallium phosphide device layer. On top of the device, layer is a 40 nm thick film of molybdenum-rhenium (MoRe). The structure is surrounded by an airbox and 1 μm underneath, a 1 μm -thick block of GaP is placed to account for the effect of the substrate. We extract a capacitance of C_{res} to be 0.17 fF. Bottom: Simulated admittance curve for the same structure. We perform a frequency-domain study where we sweep the drive frequency across the breathing mode of the resonator (Fig. 1d). From the frequencies at which the series (f_s) and parallel (f_p) resonances occur, we calculate $k_{\text{eff}}^2 = 1.59 \times 10^{-6}$.

deposited on top of the block, which result in the voltage distribution simulated in Fig. 4.

Device fabrication

Material growth. The starting material for these devices is an epitaxial structure grown by MOCVD on a GaP [110] substrate, consisting of a 1 μm thick sacrificial layer of $\text{Al}_{0.64}\text{Ga}_{0.36}\text{P}$, followed by a 230 nm thick device layer of GaP. The growth was performed in a Veeco Turbodisc D180 reactor under hydrogen as carrier gas, trimethylgallium and trimethylaluminum as organometallic precursors and under phosphine at a reactor pressure of 70 Torr.

The full device fabrication consists of two main parts: first, the patterning of the electrodes and the impedance matching circuit and second, of the optomechanical structures.

Metal layer. For the first part, we begin by spin-coating AR-P 6200-09 electron beam resist at 4000 rpm and bake it for 3 min at 160 $^{\circ}\text{C}$, followed by exposing the bond pads, ground planes, fine electrodes next to the piezoelectric resonator, and several sets of coarse and fine alignment markers for subsequent lithography steps. We then develop

the exposed resist by immersion for 1 min in pentyl acetate, followed by a 5s immersion in Xylene and a final 1 min IPA rinse. We then sputter ~40 nm of molybdenum-rhenium (MoRe) on the developed resist, followed by a lift-off step in an 80 $^{\circ}\text{C}$ bath of Anisole and gentle sonication. After the lift-off is finished, we place the sample in an IPA beaker and sonicate for 5 min, followed by blow drying.

We then spin-coat the sample with PMGI-SF11 electron-beam resist at 4000 rpm and bake it for 5 min at 190 $^{\circ}\text{C}$, followed by exposure of the scaffolding structures, which will later support the air bridges of the LC resonator. The exposed resist is then developed by immersion for 10 s in MF321 developer, 15 s H_2O , and 10 s IPA. Next, we re-flow the remaining resist by placing the sample on a pre-heated hotplate at 210 $^{\circ}\text{C}$ for 5 min.

On top of the re-flowed PMGI resist, we spin-coat AR-P 6200-18 electron-beam resist at 3250 rpm and bake at 160 $^{\circ}\text{C}$ for 3 min, followed by exposure of the spiral inductor. The resist is again developed by immersion for 1 min in Pentyl Acetate, followed by a 5s immersion in Xylene and a final 1 min IPA rinse. On the developed resist, we sputter ~90 nm of MoRe, followed by the same lift-off procedure as for the first step. The re-flowed PMGI layer is not removed by the Anisole during the lift-off and will be removed at a later time.

Device etching. For the final lithography step, we spin-coat the sample with AR-P 6200-13 at 4000 rpm followed by a bake at 160 $^{\circ}\text{C}$ for 3 min. In this lithography step, we pattern the etchmask for the photonic structures, the acoustic shielding, as well as the boundaries of the piezoelectric resonator. The resist is again developed by immersion for 1 min in Pentyl Acetate, followed by a 5s immersion in Xylene and a final 1 min IPA rinse. We transfer the etchmask to the device layer using a reactive-ion etch (RIE) step with an $\text{N}_2/\text{Cl}_2/\text{BCl}_3$ chemistry with gas flows of 10 SCCM, 20 SCCM, and 10 SCCM, respectively. We etch at a chamber pressure of 6 μbar for 1:15 min. After the RIE step, we remove the remaining etchmask along with the rest of the PMGI layer by immersion in 80 $^{\circ}\text{C}$ dimethyl-formamide (DMF) for 10 min, followed by 20 min immersion in 90 $^{\circ}\text{C}$ NMP solution. After rinsing in IPA and blow-drying, we spin-coat the sample with S1805 photoresist and use a dicing saw to cut the sample along the optical waveguides (the cut is visible in Fig. 1b) in order to provide access to the devices with a lensed optical fiber. The resist is then removed by immersion in a 50 $^{\circ}\text{C}$ Acetone bath, which is followed by an IPA rinse.

As a final fabrication step, the sacrificial $\text{Al}_{0.64}\text{Ga}_{0.36}\text{P}$ layer is selectively removed underneath the GaP device layer using a 1 h wet etch in a 10% NH_4F solution. The sample is then thoroughly rinsed in water and IPA, and dried in a critical point dryer to avoid unnecessary agitation of the suspended structures.

Simulation of the capacitance of the transducer

In the Butterworth-van Dyke (BVD) model, the piezoelectric resonator is modeled as a circuit consisting of a capacitance C_{res} , in parallel with a circuit consisting of an effective resistance R_m , inductance L_m , and capacitance C_m (see Fig. 5). For our piezoelectric resonator with modes of interest at ω_m , the product of L_m and C_m is fixed by $\omega_m = 1/\sqrt{L_m C_m}$ and the equivalent electrical resistance of the mechanical mode can be expressed as²⁷:

$$R_m = \frac{\gamma_m}{\omega_m^2} \frac{1/k_{\text{eff}}^2 - 1}{C_{\text{res}}}, \quad (2)$$

where k_{eff}^2 is the electromechanical coupling coefficient given by

$$k_{\text{eff}}^2 = \frac{C_m}{C_m + C_{\text{res}}}. \quad (3)$$

While we can determine γ_m and ω_m experimentally, the same is not true for the values of C_{res} or k_{eff}^2 . In order to contextualize the

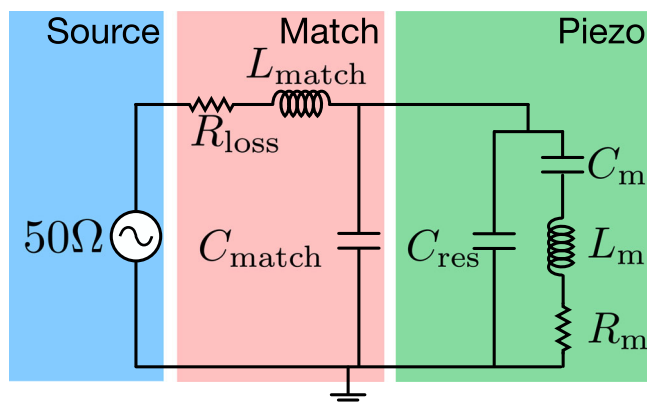


Fig. 5 | Piezo-resonator and matching circuit. Circuit representation of the electrical side of the gallium-phosphide transducer. The 50-Ω source impedance is shown in the blue area on the left. To the right, in the green region, is the piezo-resonator. This is formed of the capacitance between the superconducting plates (C_{res}), in parallel with the effective RLC-circuit formed by the electrically-active mechanical mode. On resonance with the mechanical mode, the circuit dissipates energy into the effective resistor R_m . This process can be made more efficient by impedance matching the load to the 50-Ω-source, by using a resonant LC circuit (red region) formed of a high-impedance spiral inductor (L_{match}) and the parasitic capacitance to ground (C_{match}), featuring additional resistive loss R_{loss} .

conversion results from the main text and offer potential avenues for improvement, we need to estimate the experimentally inaccessible parameters. We do this by simulating the piezoelectric resonator in COMSOL. In order to obtain the capacitance of the structure, we perform a stationary electrostatic study where we apply 1 V to the central electrode while the side electrodes are grounded (Fig. 4). Then we extract the capacitance and determine C_{res} to be 0.17 fF. In order to extract k_{eff}^2 , we perform a frequency domain study of this structure where an AC-voltage oscillating at the drive frequency is applied to the center electrode. We then extract the admittance which is shown in the bottom panel of Fig. 4. We can calculate an estimated $k_{\text{eff}}^2 = (f_p^2 - f_s^2)/f_p^2 = 1.59 \times 10^{-6}$. Owing to the small expected values of both k_{eff}^2 and C_{res} , we expect the electrical resistance of the mechanical mode, R_m to be large (2.1 MΩ for a mechanical quality factor of 1×10^5), such that it is inefficiently excited from at 50-Ω source impedance. To help overcome this expected impedance mismatch, we include a superconducting impedance matching resonator (red area in Fig. 5). More details can be found in the *Methods*.

OMC-Waveguide coupling

We access the optical photons in our transducer through an evanescently coupled waveguide (see Fig. 1c of the main manuscript). The optical resonator is coupled to the waveguide at a rate κ_e , and features an intrinsic loss rate κ_i , resulting in a total loss rate $\kappa = \kappa_e + \kappa_i$ and limiting the interface efficiency to the overcoupling ratio: $\eta_o = \kappa_e / (\kappa_e + \kappa_i)$. We can directly access these rates through monitoring the phase of resonant light reflected from the cavity. To do this, we set a laser tone at a fixed detuning a few Gigahertz from the optical resonance, and scan the frequency of a microwave tone we send to an amplitude EOM. The tone results in our detuned carrier tone, E_0 and two in-phase sidebands, E_{\pm} , of which E_- is resonant with the cavity. Each of these tones is reflected from the cavity with coefficient r , given by:

$$r = 1 - \frac{\kappa_e}{\kappa/2 - 2i\Delta}, \quad (4)$$

where $\Delta = \omega_l - \omega_c$ is the detuning of the particular tone at frequency ω_l from the cavity resonance at ω_c . We detect the components of the

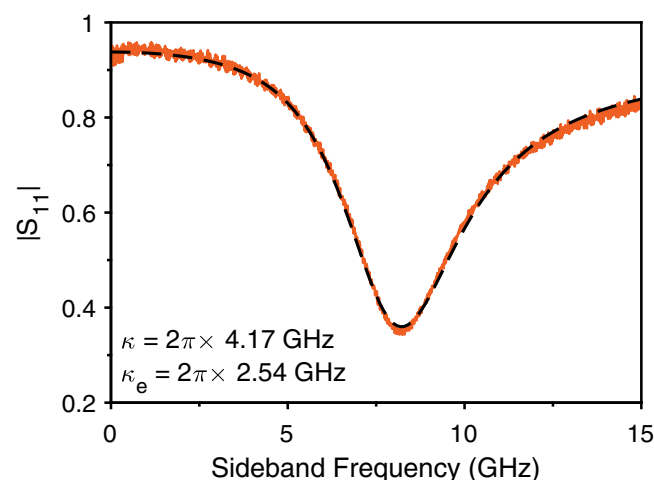


Fig. 6 | Characterization of the optical cavity. The orange curve is the reflection parameter from the optical cavity. We stabilize a laser 8-GHz blue-detuned from the optical resonance and scan GHz-frequency sidebands across the optical resonance. For an over-coupled device, the reflected light from the two sidebands interferes destructively and the value of $|S_{11}|$ dips below 0.5. The dashed black curve is a fit for the data.

reflected signal at the same frequency as our microwave drive resulting in the complex scattering parameter:

$$S_{11} = E_0 E_+^* + E_0^* E_+ + E_0 E_-^* + E_0^* E_-, \quad (5)$$

with each tone being reflected by its own value of r . Figure 6 shows the calibrated value of $|S_{11}|$ for the device measured in the main text. We fit the data according to Eqs. (4) and (5), with the intrinsic loss rate, the external coupling rate and the exact detuning of the carrier tone E_0 as free parameters. We recover a total cavity linewidth of $\kappa = 2\pi \times 4.17$ GHz, and an external coupling rate $\kappa_e = 2\pi \times 2.54$ GHz, from which we extract an optical interface efficiency of $\eta_o = 0.61$, which is the out-coupling efficiency from the optical resonator to the nearby waveguide.

Scattering probabilities

In order to examine the different contributions to the overall device efficiency we need to estimate the optomechanical efficiency of the interface $\eta_{\text{om}} = p_{\text{sw}} \eta_o$, where p_{sw} is the probability of converting a phonon to an optical-frequency photon in the resonator, and $\eta_o = 0.61$. We can estimate the scattering probability, p_{sw} from³⁹:

$$p_{\text{sw}} = 1 - \exp\left(\frac{-4\eta_o g_0^2 E_p}{\hbar\omega_l (\omega_m^2 + (\kappa/2)^2)}\right), \quad (6)$$

where g_0 is the single photon optomechanical coupling strength, E_p the red-detuned pulse energy at frequency $\omega_l = \omega_c - \omega_m$ and ω_m the frequency of the mechanical mode.

In order to calibrate the optical pulse energy we measure the coupling of our optical fiber to the device waveguide from the reflection of probe light 100 GHz detuned from the optical resonance. We measure this value to be $\eta_{\text{coup}} = 0.50$. We can estimate the value of g_0 from the power-dependent damping rate displayed in Fig. 2d. We fit the FWHM of the conversion peak and use the following expression for the power-dependent optomechanical damping rate⁴⁰:

$$\gamma_m = \gamma_{m,0} + n_c g_0^2 (\mathcal{L}_+ - \mathcal{L}_-), \quad (7)$$

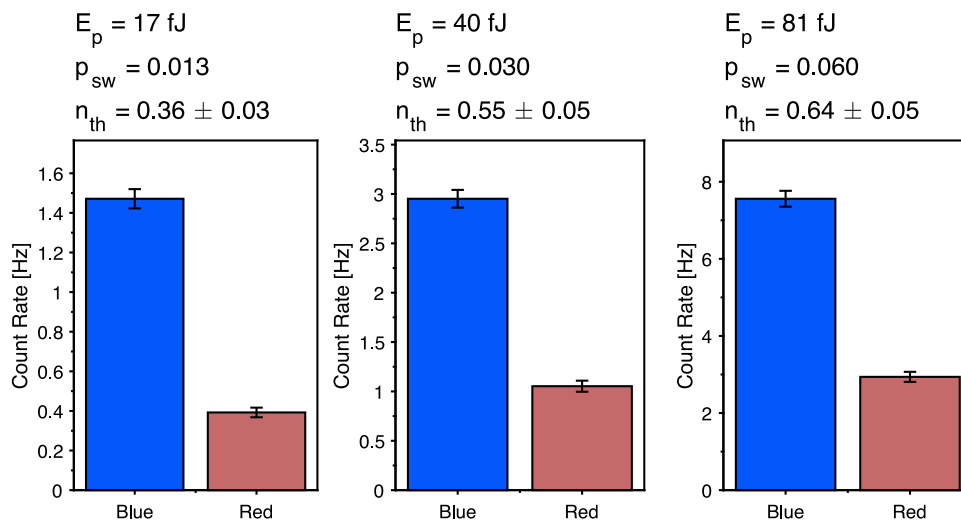


Fig. 7 | Sideband asymmetry. Recorded countrates for scattering from the blue and red sidebands of the optical device for different pulse energies. The scattering probability p_{sw} is calculated for the mode at 2.799 GHz. For higher pulse energies,

the scattering probability increases, but with increasing thermal noise due to absorption. Error bars are s.d.

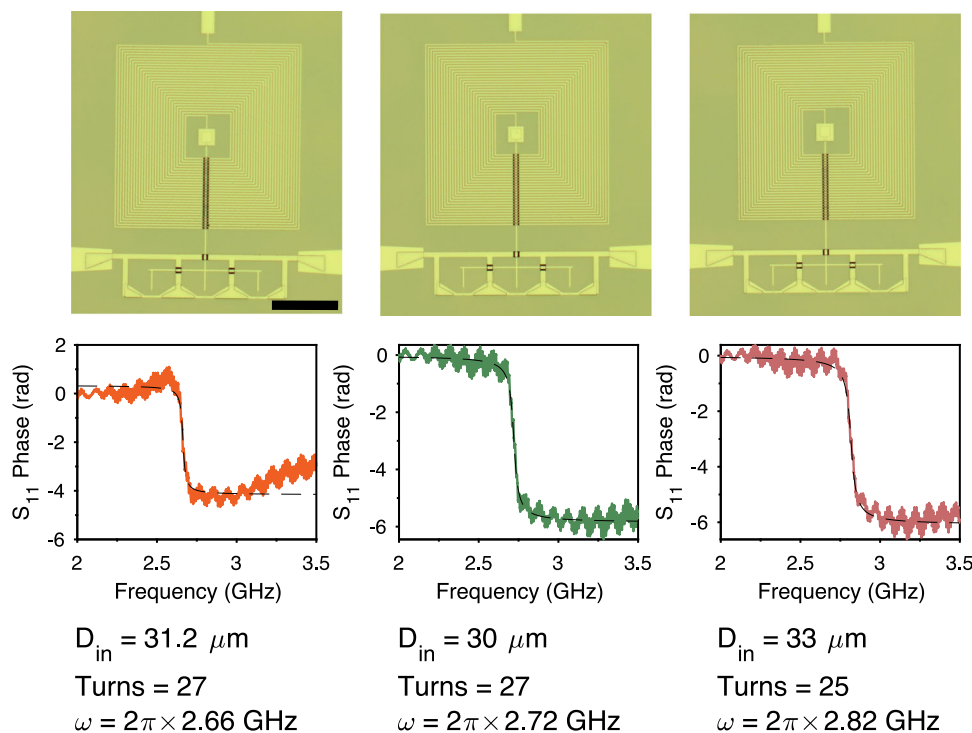


Fig. 8 | Inductor characterization. Top row: Microscope images of three test inductors aimed at targeting the mechanical resonance frequency. The scale bar in the left image is 200 μm . Bottom row: Phase response of the test inductors

measured at 4 K. The text labels show the inner diameter of the inductor, the number of turns, and fitted resonance frequency of the devices. Note, due to technical reasons the phase response for the device on the left is slightly reduced.

where Δ is the detuning of the optical pump from the cavity resonance, ω_m and $\gamma_{m,0}$ is the zero-power linewidth, and \mathcal{L}_{\pm} is given by:

$$\mathcal{L}_{\pm} = \frac{\kappa}{\kappa^2/4 + (\Delta \pm \omega_m)^2}. \quad (8)$$

For the mode at 2.799 GHz, we find this value to be $g_0 = 2\pi \times 700 \pm 8$ kHz, while for the mode at 2.790 GHz, we fit a lower value of $2\pi \times 272 \pm 14$ kHz.

The scattering probability increases for larger optical pulse powers, however results in an increased thermal population of the

mechanical mode, due to optical absorption. Figure 7 displays the measured sideband asymmetry for three optical pulse powers, as well as the extracted thermal population, and the scattering probability from the 2.799 GHz mode. We use a power of 40 fJ in the main manuscript, corresponding to a thermal population of $n_{th} = 0.55 \pm 0.05$ and a scattering probability of 0.03.

It also is important to note that our device is not fully in the resolved sideband regime ($\omega_m/\kappa = 0.67$), and as a result there is a non-negligible probability for Stokes-scattering from a red-detuned optical pulse. The amount of undesired Stokes scattering from our device can be estimated to be $0.12 \times p_{sw}^{27}$. In the pulsed protocol used in Fig. 3, we

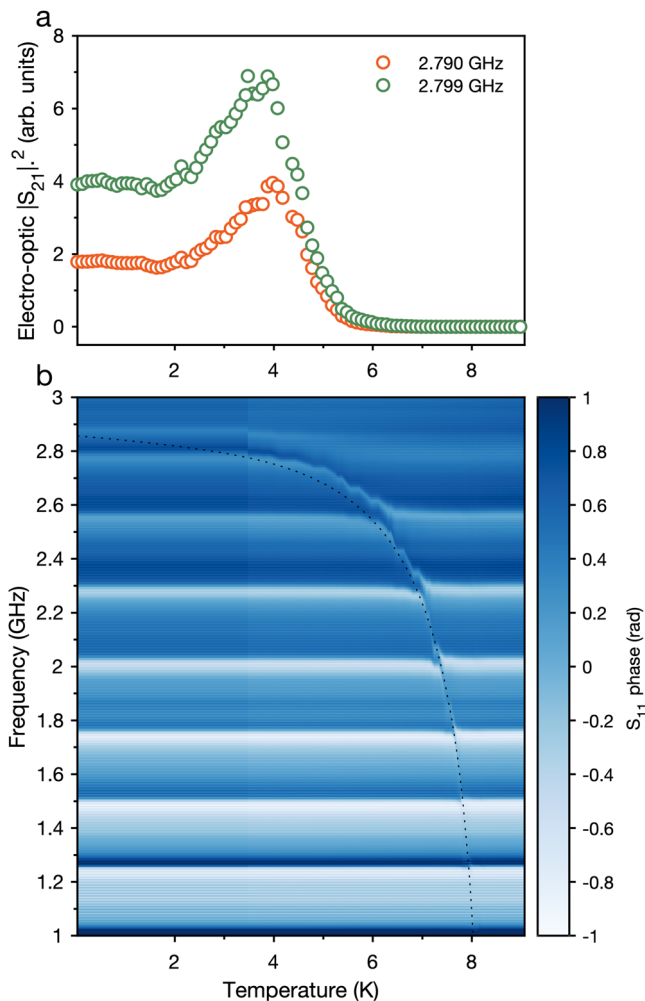


Fig. 9 | Electro-mechanical interface. **a** The evolution in the electro-optic scattering parameter as the device temperature is increased from 20 mK up to 9 K. Displayed are the signal sizes for the modes at 2.790 and 2.799 GHz. **b** The phase of the reflected signal from the microwave port of the device for the same temperature range. This data was recorded simultaneously with the electro-optic data in **a**. The dotted curve is a fit to the impedance-matching circuit resonance frequency, from the BCS theory of kinetic inductance as the film approaches the critical temperature.

only measure scattered photons at the cavity resonance, selecting the 89% of scattering events that result from the beam-splitter interaction. One consequence of imperfect sideband resolution is amplification-induced noise from the non-suppressed two-mode-squeezing interaction. We note that this noise source is limited to a value of $0.12 \times p_{\text{sw}}$, which for the pulse energies used in Fig. 3 is <0.01 phonons, and can be neglected in comparison to absorption-induced noise.

Piezoelectric interface

We construct our resonant impedance matching circuit from a thin-film spiral inductor, with the stray capacitance to ground forming the LC-circuit shown in Fig. 5. We deposit a film of 90-nm thick MoRe in a square spiral, with track width and spacing of 1 μm . We use airbridge crossovers to route the signal out from the center of the spiral. For the device in the main text, we use a 27-turn inductor with an inner diameter of 30 μm .

Figure 8 shows microscope images and phase-response from three test inductors fabricated on bulk gallium phosphide, tested at 4 K. The devices show overcoupled resonances close to the target mechanical frequency. Fitting the response of the standard (50- Ω -

coupled) RLC circuit reveals a capacitance of ≈ 19 fF, with an inductance of 180 nH. The capacitance is slightly larger than the simulated limit of these devices at 12.6 fF. The capacitance of these circuits could be further reduced by reducing the size of the track width and film thickness, however this optimization requires further fabrication development to achieve a reliable fabrication process. The impedance-matching resonators are directly connected to the 50- Ω input line, resulting in overcoupled resonators with quality factors of 62, and impedances of $Z_{\text{match}} = \sqrt{L/C} = 3.1$ k Ω . We find that any additional resistive losses R_{loss} amount to only 2–4 Ω , small enough to be neglected in comparison to the 50- Ω source impedance.

We expect the thin-film devices at Millikelvin temperatures to show higher-frequency resonances by ~ 90 MHz, with a blue shift of 30 MHz due to the lower dielectric constant of the AlGaP sacrificial layer⁴¹ and a blue-shift of 60 MHz due to the reduced kinetic inductance at lower temperature.

Figure 9 displays the result of a temperature sweep of the device, performed by raising the temperature of the dilution fridge cold plate, during which we continuously measure the electro-optic signal, in the same style as in Fig. 2, as well as the reflected microwave signal. The microwave resonator is partially obscured by reflections in the microwave line, however as the temperature is increased to 8 K, we observe a red-shift of the resonance frequency, consistent with an increasing kinetic inductance in the MoRe film as we approach the critical temperature. The dotted curve in Fig. 9b displays a fit of the resonance frequency according to the BCS theory of the change in kinetic inductance near the critical temperature⁴², which reproduces the reduction in resonance frequency we observe.

One effect of the increase in film-kinetic inductance is the change of detuning between the mechanical-mode frequencies and the impedance-matching resonance. Figure 9a displays the electro-optic signal measured for the mechanical modes at 2.790 and 2.799 GHz through the temperature sweep. We record an increase in the efficiency (proportional to $|S_{21}|^2$) of the transducer as the electrical resonance passes the two mechanical modes at around 4 K. Above this temperature the impedance matching resonance rapidly decreases below 2.79 GHz and the efficiency reduces.

Bi-directional conversion

The linear conversion process between the microwave and optical domains with our platform is bi-directional, as can be seen in Fig. 10. Here, we also observe down-conversion from optical to microwave frequencies in an analogous way to the up-conversion shown in Fig. 2 of the main text. We generate a signal to be down-converted by modulating our red-detuned pump laser with an electro-optic modulator at around 3 GHz. We then directly detect the output microwave signal from the transducer using a cryogenically cooled HEMT amplifier at the 4-K stage of the dilution fridge. The results for both up-conversion and down-conversion for varying optical pump power are displayed in Fig. 10. Due to technical reasons, the data were taken using a different device on the same chip as the device in the main manuscript which is in principle identical, except for featuring an inductor with 26 turns and an internal diameter of 31.5 μm , and featuring a peak in transduction efficiency at 2.807 GHz. While up-conversion and down-conversion occur with the same efficiency, the reduced signal-to-noise in the down-conversion stems from the smaller efficiency in the microwave-frequency detection path.

With bi-directional conversion, we can calibrate the losses in the microwave and optical lines to estimate the conversion efficiency. In order to do this, we extract the off-resonant reflection of optical and microwave tones from the device, to provide $S_{\text{OO,bgd}}$ and $S_{\text{EE,bgd}}$, respectively. We fit the transduced fields with square-root Lorentzian profiles, following the expected transduction profile. The fitted amplitudes for up-conversion and down-conversion ($S_{\text{OE,pk}}$ and $S_{\text{EO,pk}}$, respectively) are plotted in Fig. 10e, f. From these four values,

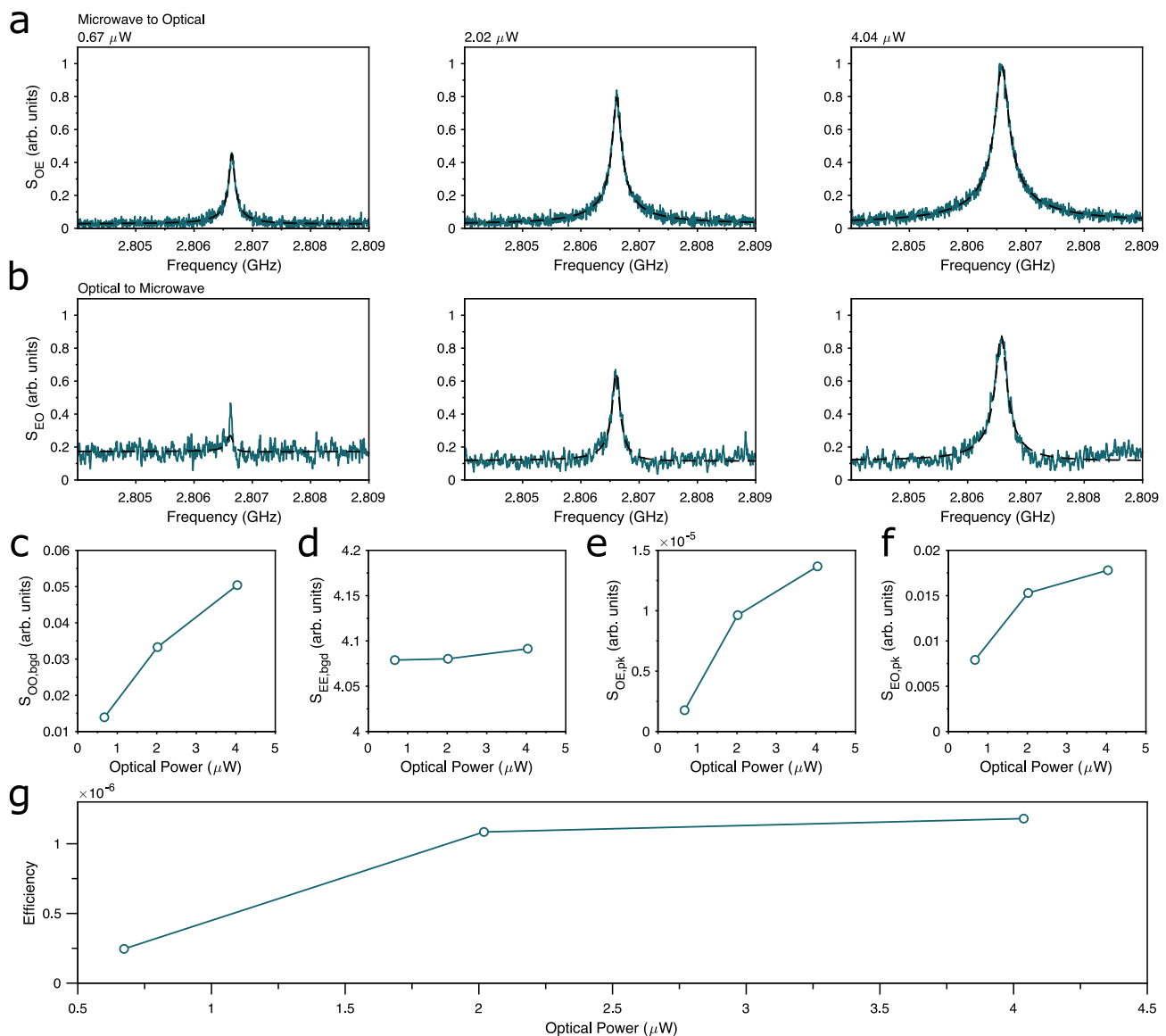


Fig. 10 | Bi-directional transduction in gallium phosphide. Top Row: Microwave-to-optical transduction measured for varying optical input power. Second Row: Optical-to-microwave transduction measured for the same device under the same optical pump powers. Third Row: Background and extracted peak values for optical and microwave reflection, upconversion, and downconversion. Bottom Row: Estimated Conversion efficiency.

we can estimate the efficiency by

$$\eta = \frac{S_{OE, pk} S_{EO, pk}}{S_{OO, bgd} S_{EE, bgd}} \quad (9)$$

The extracted efficiency estimates for the three measured pump powers are displayed in Fig. 10g. These values show good agreement with pulsed efficiencies extracted for this device, for which we measure an electrical-to-mechanical per-photon efficiency of 3.4×10^{-6} .

Data availability

Source data for the plots are available at <https://doi.org/10.5281/zenodo.7191940>.

References

- Arute, F. et al. Quantum supremacy using a programmable superconducting processor. *Nature* **574**, 505 (2019).
- Veldhorst, M. et al. A two-qubit logic gate in silicon. *Nature* **526**, 410 (2015).
- Hendrickx, N. W. et al. A four-qubit germanium quantum processor. *Nature* **591**, 580 (2021).
- Yu, Y. et al. Entanglement of two quantum memories via fibres over dozens of kilometres. *Nature* **578**, 240 (2020).
- Nagayama, K., Kakui, M., Matsui, M., Saitoh, T. & Chigusa, Y. Ultra-low-loss (0.1484 db/km) pure silica core fiber and extension of transmission distance. *Electron. Lett.* **38**, 1168 (2002).
- Chang, J. et al. Detecting telecom single photons with $99.5^{+0.5}_{-2.07}\%$ system detection efficiency and high time resolution. *APL Photonics* **6**, 036114 (2021).
- Zeuthen, E., Schliesser, A., Sørensen, A. S. & Taylor, J. M. Figures of merit for quantum transducers. *Quantum Sci. Technol.* **5**, 34009 (2020).
- Zhong, C. et al. Proposal for heralded generation and detection of entangled microwave-optical-photon pairs. *Phys. Rev. Lett.* **124**, 10511 (2020).
- Krastanov, S. et al. Optically-heralded entanglement of superconducting systems in quantum networks. *Phys. Rev. Lett.* **127**, 040503 (2021).

10. Lauk, N. et al. Perspectives on quantum transduction. *Quantum Sci. Technol.* **5**, 20501 (2020).
11. Hease, W. et al. Bidirectional electro-optic wavelength conversion in the quantum ground state. *PRX Quantum* **1**, 020315 (2020).
12. Bagci, T. et al. Optical detection of radio waves through a nano-mechanical transducer. *Nature* **507**, 81 (2014).
13. Balram, K. C., Davanço, M. I., Song, J. D. & Srinivasan, K. Coherent coupling between radiofrequency, optical and acoustic waves in piezo-optomechanical circuits. *Nat. Photon.* **10**, 346 (2016).
14. Higginbotham, A. P. et al. Electro-optic correlations improve an efficient mechanical converter. *Nat. Phys.* **14**, 1038 (2018).
15. Han, X. et al. Cavity piezo-mechanics for superconducting-nanophotonic quantum interface. *Nat. Commun.* **11**, 3237 (2020).
16. Jiang, W. et al. Efficient bidirectional piezo-optomechanical transduction between microwave and optical frequency. *Nat. Commun.* **11**, 1166 (2020).
17. Arnold, G. et al. Converting microwave and telecom photons with a silicon photonic nanomechanical interface. *Nat. Commun.* **11**, 4460 (2020).
18. Peairs, G. A. et al. Continuous and time-domain coherent signal conversion between optical and microwave frequencies. *Phys. Rev. Appl.* **14**, 1 (2020).
19. Riedinger, R. et al. Non-classical correlations between single photons and phonons from a mechanical oscillator. *Nature* **530**, 313 (2016).
20. Riedinger, R. et al. Remote quantum entanglement between two micromechanical oscillators. *Nature* **556**, 473 (2018).
21. Wallucks, A., Marinković, I., Hensen, B., Stockill, R. & Gröblacher, S. A quantum memory at telecom wavelengths. *Nat. Phys.* **16**, 772 (2020).
22. O'Connell, A. D. et al. Quantum ground state and single-phonon control of a mechanical resonator. *Nature* **464**, 697 (2010).
23. Chu, Y. et al. Creation and control of multi-phonon fock states in a bulk acoustic-wave resonator. *Nature* **563**, 666 (2018).
24. Mirhosseini, M., Sipahigil, A., Kalaei, M. & Painter, O. Superconducting qubit to optical photon transduction. *Nature* **588**, 599 (2020).
25. Wilson, D. J. et al. Integrated gallium phosphide nonlinear photonics. *Nat. Photon.* **14**, 57 (2020).
26. Stockill, R. et al. Gallium phosphide as a piezoelectric platform for quantum optomechanics. *Phys. Rev. Lett.* **123**, 163602 (2019).
27. Wu, M., Zeuthen, E., Balram, K. C. & Srinivasan, K. Microwave-to-optical transduction using a mechanical supermode for coupling piezoelectric and optomechanical resonators. *Phys. Rev. Appl.* **13**, 014027 (2020).
28. Eichenfield, M., Chan, J., Camacho, R. M., Vahala, K. J. & Painter, O. Optomechanical crystals. *Nature* **462**, 78 (2009).
29. Schneider, K. et al. Optomechanics with one-dimensional gallium phosphide photonic crystal cavities. *Optica* **6**, 577 (2019).
30. Fang, K. et al. Generalized non-reciprocity in an optomechanical circuit via synthetic magnetism and reservoir engineering. *Nat. Phys.* **13**, 465 (2017).
31. MacCabe, G. S. et al. Nano-acoustic resonator with ultralong phonon lifetime. *Science* **370**, 840 (2020).
32. Singh, V., Schneider, B. H., Bosman, S. J., Merks, E. P. J. & Steele, G. A. Molybdenum-rhenium alloy based high-Q superconducting microwave resonators. *Appl. Phys. Lett.* **105**, 222601 (2014).
33. Samkharadze, N. et al. High-kinetic-inductance superconducting nanowire resonators for circuit QED in a magnetic field. *Phys. Rev. Appl.* **5**, 044004 (2016).
34. Xu, M., Han, X., Fu, W., Zou, C.-L. & Tang, H. X. Frequency-tunable high-Q superconducting resonators via wireless control of non-linear kinetic inductance. *Appl. Phys. Lett.* **114**, 192601 (2019).
35. Peruzzo, M., Trioni, A., Hassani, F., Zemlicka, M. & Fink, J. M. Surpassing the resistance quantum with a geometric superinductor. *Phys. Rev. Appl.* **14**, 044055 (2020).
36. Hönl, S. et al. Microwave-to-optical conversion with a gallium phosphide photonic crystal cavity. *Nat. Commun.* **13**, 2065 (2022).
37. Soderkvist, J. & Hjort, K. The piezoelectric effect of GaAs used for resonators and resonant sensors. *J. Micromech. Microeng.* **4**, 28 (1994).
38. Nelson, D. F. & Turner, E. H. Electro-optic and piezoelectric coefficients and refractive index of gallium phosphide. *J. Appl. Phys.* **39**, 3337 (1968).
39. Hong, S. et al. Hanbury Brown and Twiss interferometry of single phonons from an optomechanical resonator. *Science* **358**, 203 (2017).
40. Aspelmeyer, M., Kippenberg, T. J. & Marquardt, F. Cavity optomechanics. *Rev. Mod. Phys.* **86**, 1391 (2014).
41. Robert, C. et al. Structural and optical properties of AlGaP confinement layers and InGaAs quantum dot light emitters onto GaP substrate: towards photonics on silicon applications. *Thin Solid Films* **541**, 87 (2013).
42. Annunziata, A. J. et al. Tunable superconducting nanoinductors. *Nanotechnology* **21**, 445202 (2010).

Acknowledgements

We would like to thank Mario Gely, Bas Hensen, Marios Kounalakis, Igor Marinković, Sarwan Peiter, Felix Schmidt, Kartik Srinivasan and Andreas Wallucks for valuable discussions and support. We also acknowledge assistance from the Kavli Nanolab Delft. This work is supported by the French RENATECH network (I.S., R.B.), as well as by the Foundation for Fundamental Research on Matter (FOM) Projectruimte grant (16PR1054) (S.G.), the European Research Council (ERC StG Strong-Q, 676842 and ERC CoG Q-ECHOS, 101001005) (S.G.), and by the Netherlands Organization for Scientific Research (NWO/OCW) (S.G.), as part of the Frontiers of Nanoscience program, as well as through Vidi (680-47-541/994) (S.G.) and Vrij Programma (680-92-18-04) (S.G.) grants. R.S. also acknowledges funding from the European Union under a Marie Skłodowska-Curie COFUND fellowship.

Author contributions

R.S., M.F., and S.G. planned the experiment and performed the device design. G.B., K.P., I.S., and R.B. supplied the material. R.S. and M.F. fabricated the sample and R.S., M.F., and F.H. performed sample characterization. R.S. and M.F. performed the measurements, while R.S., M.F., and S.G. analyzed the data and wrote the manuscript with input from all authors. S.G. supervised the project.

Competing interests

R.S., F.H., and S.G. declare a financial interest in QphoX B.V. The remaining authors declare no other competing interests.

Additional information

Correspondence and requests for materials should be addressed to Simon Gröblacher.

Peer review information *Nature Communications* thanks the anonymous reviewer(s) for their contribution to the peer review of this work.

Reprints and permissions information is available at <http://www.nature.com/reprints>

Publisher's note Springer Nature remains neutral with regard to jurisdictional claims in published maps and institutional affiliations.

Open Access This article is licensed under a Creative Commons Attribution 4.0 International License, which permits use, sharing, adaptation, distribution and reproduction in any medium or format, as long as you give appropriate credit to the original author(s) and the source, provide a link to the Creative Commons license, and indicate if changes were made. The images or other third party material in this article are included in the article's Creative Commons license, unless indicated otherwise in a credit line to the material. If material is not included in the article's Creative Commons license and your intended use is not permitted by statutory regulation or exceeds the permitted use, you will need to obtain permission directly from the copyright holder. To view a copy of this license, visit <http://creativecommons.org/licenses/by/4.0/>.

© The Author(s) 2022